

# Chapter 2

## Radon-Wigner Display

### 2.1 Introduction

In some situations it is not possible, or not desirable, to perform a full characterization of the spatial structure of 2D beams since under certain hypothesis the analysis of 1D beam profiles is more convenient. This is the case of, for example, the spatial coherence study of X-ray sources [She91, Dit96] and rotationally invariant 2D beams, whose WD can be reconstructed from the WD of one of its radial profiles [Aga00]. Therefore, the characterization of 1D beams, which is significantly easier than the characterization of 2D beams, is an important problem with relevant applications.

A 1D beam is described by its complex field amplitude,  $f(x)$ . Therefore, its MI,  $\Gamma(x_1, x_2)$ , and WD,  $W(x, u)$ , are 2D functions. This simplifies the acquisition, storage, and processing of the WD projections, which can be performed using standard computer technology. In fact, considering the information contained in a WD stored in a multiarray of  $N = 256$  sampling points per dimension of double precision (8 B), the 32 GiB needed for the 2D case is reduced to 512 KiB in the 1D case. Furthermore, there exist several optical systems [Men96, Gra97, Zha98] suitable for the acquisition in a single measurement of the full-range RWT of the 1D beam. These systems are commonly referred to as RWD.

In this chapter we present a RWD that provides several advantages compared with other RWDs proposed in the literature. Our setup relies in SLMs, which are electronically addressable optical elements introduced in Sect. 2.2. The suggested RWD is presented in Sect. 2.3. It allows measuring the beam RWT for tunable angular range as the intensity distribution at the output plane of the system. In order to experimentally demonstrate the feasibility of our RWD, the WD of several signals are recovered from their measured RWTs in Sect. 2.4. In particular, the extraction of the defining parameters of a windowed chirp signal are studied using different methods. Finally, the WD of the 1D projection of a HG beam and a radial profile of a coherent rotationally invariant 2D beam are reconstructed using the RWD.

## 2.2 Spatial Light Modulators for Lens Implementation and Beam Generation

A SLM is an optical device that modifies the beam intensity and phase distributions. The term was originally coined to describe static elements like phase retarders or amplitude filters. These devices convert an input beam described by  $f_i(\mathbf{r})$  into [Goo05]

$$f_o(\mathbf{r}) = f_i(\mathbf{r}) t(\mathbf{r}), \quad (2.1)$$

where

$$t(\mathbf{r}) = t_A(\mathbf{r}) \exp[i\Psi(\mathbf{r})] \quad (2.2)$$

is the transmission function,  $t_A$  is the real function taking values in the range  $[0, 1]$  referred to as amplitude transmission, and  $\Psi$  is a real function defining the phase modulation. Nowadays, the SLMs based on the liquid crystal on silicon technology can be electronically addressed to dynamically control its modulation properties over time. With the aid of a computer, the transmission function of modern SLMs can be updated at rates around 60 Hz, which make them useful for many applications including adaptive optics in astronomy [Bon90], data storage [Oht99], microscopy [Nei00], or micro-object manipulation using optical tweezers [Wul06]. SLMs are of special importance in this dissertation for the realisation of two tasks: implementing digital lenses with controllable focal length and generating beams with arbitrary spatial structure using computer-generated holograms. For the sake of simplicity, and unless otherwise stated, we will refer with SLM to electronically addressable SLMs using liquid crystal on silicon technology.

The display of a SLM is its optical sensitive element, i.e. the element that actually modulates the beam. It is composed by a 2D array of independent cells or pixels. Each pixel behaves like a neutral density filter or phase retarder—depending on whether the SLM is working in amplitude or phase modulation—independently controllable from a computer. In the case of an amplitude-only SLM the pixel can take values in the range  $[0, 1]$ , where the values 0 and 1 correspond to opaque and completely transparent filters, respectively. Conversely, in the case of a phase-only SLM the pixel can usually retard the beam in a full  $2\pi$ -range interval, although in some situations a smaller or larger range can be addressed. Every pixel may only take concrete values contained in the SLM dynamic range, usually formed by 256 values. Commonly, SLMs are specialized in modifying the amplitude or phase of the beam, not both at the same time. In addition, depending on whether the modified beam is transmitted through or reflected from the device, the SLMs are further classified into transmission and reflection SLMs. Unless otherwise stated, we will assume reflection SLMs operating in phase-only modulation regime for a full  $2\pi$ -range interval when referring to SLMs.

An interesting application of SLMs is the implementation of thin lenses of variable focal length. A thin lens can be considered a transmission phase mask with quadratic phase modulation function. For example, a spherical lens of focal length  $f$  is described in thin-lens and paraxial approximation by the phase mask [Goo05],

$$t(\mathbf{r}) = \exp \left[ -\frac{i\pi}{\lambda f} (x^2 + y^2) \right], \quad (2.3)$$

where  $\lambda$  is the wavelength of the incident light. This kind of lenses can be digitally implemented by phase-only SLMs. Notice that since the SLM is formed by pixels with finite size that are separated by a certain distance, the phase transmission can only be correctly implemented in the areas where the phase oscillations are not very rapid in order to satisfy the Nyquist sampling theorem [Goo05]. Consider the phase modulation function for a thin-lens defined by Eq. (2.3), which is displayed in Fig. 2.1 for  $\lambda = 532$  nm and focal lengths of 0.75 and 0.25 m. The phase difference between two consecutive horizontal pixels with positions  $k$  and  $k + 1$  is given by

$$\Delta\Psi_k = \Psi[(k+1)\Delta x] - \Psi(k\Delta x) = \pi(2k+1) \frac{(\Delta x)^2}{\lambda f}, \quad (2.4)$$

where  $\Delta x$  is the separation between pixels, also known as pixel pitch. If the phase difference is below half a phase cycle, i.e.  $\Delta\Psi_k < \pi$ , there are more than two samples per phase cycle and the phase amplitude is well-sampled according to the Nyquist theorem. On the contrary, if the phase difference is above half cycle then the phase modulation is sampled with less than two samples per cycle and, therefore, the phase is undersampled. In order to assure the quality of the lenses we impose a more restrictive sampling condition. Instead of using two pixels per cycle, we require six pixels per cycle to consider the phase mask well sampled. Since we discard the

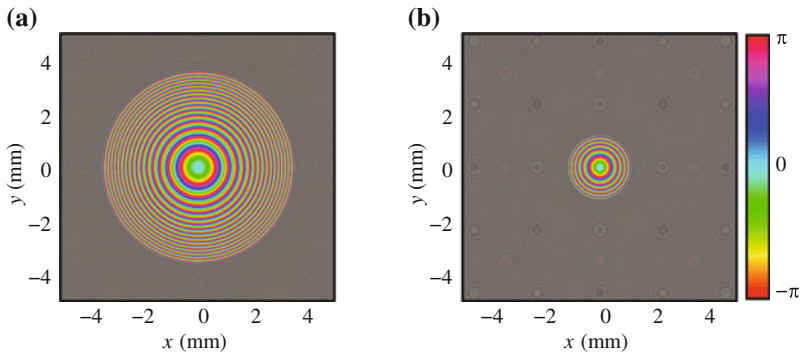


**Fig. 2.1** Phase modulation corresponding to thin-lenses of focal lengths **a** 0.75 m and **b** 0.25 m. When using a SLM with pixel pitch  $18 \mu\text{m}$ , the shaded areas are sampled with a rate below 6 pixels per cycle and are not used to avoid their associated optical aberrations. Notice that reducing the focal length of the digital lens reduces its effective aperture

light that falls into the areas where this condition is not satisfied, each digital lens has a virtual circular aperture of size  $k_{\text{lim}}\Delta x$ , where

$$\Delta\Psi_{k_{\text{lim}}} = \pi/3 \Rightarrow k_{\text{lim}} = \frac{1}{3} \left[ \frac{\lambda f}{2(\Delta x)^2} - 1 \right]. \quad (2.5)$$

These apertures are present in Fig. 2.1 for a SLM of pixel pitch  $18\text{ }\mu\text{m}$ . Notice that this means that reducing the focal length of the digital lens reduces its virtual aperture. In all the experiments of the dissertation where digital lenses are involved we have checked that the generated signals fall into the sufficiently sampled zones.

Apart from the digital lenses, SLMs can implement phase-only CGHs for the high-fidelity generation of coherent beams with on-demand amplitude and phase distributions [Arr07]. The technique consists in illuminating a phase mask, the hologram, with a reference beam, usually an approximation of a plane wave. In our case the expanded, filtered, and collimated Gaussian beam of a laser source is used for this goal, see Fig. 2.2. When the waist of the Gaussian is significantly wider than the signal to be generated, its central region can be approximated to a plane wave. The hologram converts the reference beam into a beam whose Fourier expansion with respect to the phase distribution,  $\phi(\mathbf{r})$ , contains a term that is the desired beam. In order to obtain in the first term of the Fourier expansion the signal described by

$$f(\mathbf{r}) = a(\mathbf{r}) \exp[i\phi(\mathbf{r})], \quad (2.6)$$

where  $a$  and  $\phi$  are its amplitude and phase distributions, the phase modulation function,  $h(\mathbf{r}) = \exp[i\Psi(\mathbf{r})]$ , that satisfies the following relations has to be found [Arr07]

$$\Psi(\mathbf{r}) = g[a(\mathbf{r})]\phi(\mathbf{r}), \quad (2.7)$$

$$\text{sinc}\{1 - g[a(\mathbf{r})]\} = a(\mathbf{r}), \quad (2.8)$$

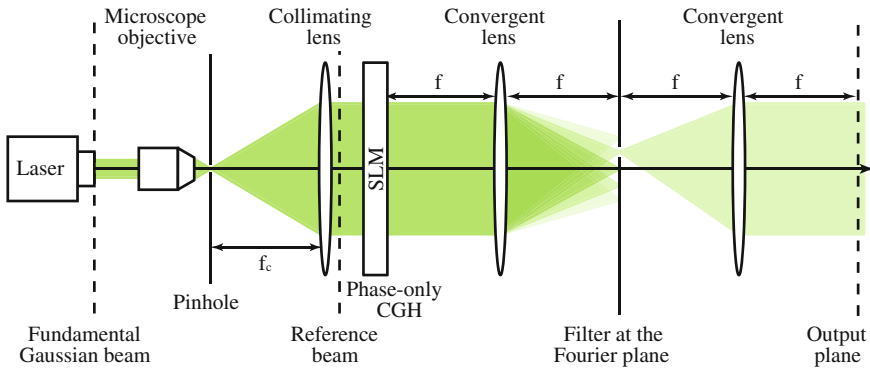


**Fig. 2.2** Scheme of the optical system used for the signal generation using phase-only computer generated holography

where  $\text{sinc}(\mathbf{r}) = \sin(\pi x) \sin(\pi y) / (\pi^2 xy)$  and  $g$  is an arbitrary function that depends on the amplitude distribution. The solution for  $g$  has no analytic expression; hence it has to be numerically inverted from Eq. (2.8).

The conditions given by Eqs. (2.7) and (2.8) define a special kind of CGH referred to as CGH of type I in [Arr07]. There are alternative ways to construct the hologram, see for instance the type II and III CGHs of [Arr07], that provide higher-fidelity on the generated beam. We will use type I CGHs throughout the dissertation, however, due to their greater energy efficiency and because they do not require additional masks on the SLM for its implementation.

The generated signal contains all the Fourier series terms, including the desired beam  $f(\mathbf{r})$ ,

$$h(\mathbf{r}) = \sum_m C_m [a(\mathbf{r})] \exp [im\phi(\mathbf{r})], \quad (2.9)$$

where  $C_m$  are the expansion coefficients which depend on the amplitude  $a(\mathbf{r})$ . In order to isolate the desired signal, corresponding to the first term, we include a carrier in the phase distribution of  $f$ :

$$f(\mathbf{r}) \longrightarrow f(\mathbf{r}) \exp (i2\pi \mathbf{r} \cdot \mathbf{k}_c), \quad (2.10)$$

where  $\mathbf{k}_c = (k_{x,c}, k_{y,c})$  is the carrier frequency. The  $q$ th order Fourier term is affected by a carrier of frequency  $q\mathbf{k}_c$ . Therefore, each expansion term is spatially separated at the Fourier plane of a 4-f telescopic system [Goo05], where all the terms except the  $q = 1$  are filtered. In addition, due to the pixelated nature of the SLM, other diffraction orders appear at the Fourier plane, complicating the filtering of the desired term. An illustration of the different orders present at the Fourier plane is displayed in Fig. 2.3. Also consider that the suppression of most of the terms present at the Fourier plane makes CGH an energetically inefficient technique. Despite these inconveniences, CGHs excel at the generation of beams with arbitrary and dynamically-changeable phase and amplitude distributions. The scheme of this optical system is displayed in Fig. 2.2.

Although the higher the carrier frequency the easier it is to filter the undesired terms in the Fourier plane, it is not possible to choose carriers with arbitrary frequencies; they are limited by the Nyquist sampling theorem just like the focal length of digital lenses. For the case of a SLM with pixel pitch of  $8 \mu\text{m}$ , the limiting carrier frequency according to Nyquist theorem is two pixels per cycle,  $k_{x,0} \sim k_{y,0} \sim 60 \text{ mm}^{-1}$ . In order to assure the quality of the carrier, however, we used in the experiments a lower frequency carrier of six pixels per cycle,  $k_{x,0} \sim k_{y,0} \sim 20 \text{ mm}^{-1}$ .

These two applications – the phase-mask implementation and beam generation – will be used throughout the dissertation. In particular, as we will see in the following Sections, the RWD proposed by us uses SLMs to augment its versatility, producing important advantages.

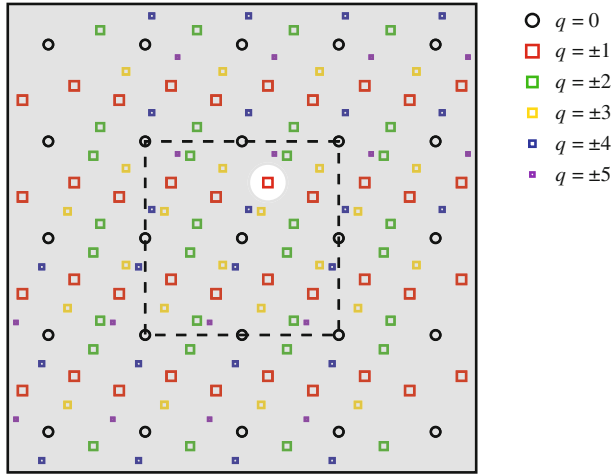


**Fig. 2.3** Illustration of the different contributions obtained in the Fourier plane of the 4-f telescope for a typical CGH. *Black circles* represent the zero-order term of the Fourier expansion, while *coloured squares* represent the different expansion orders. *Squares* have different size depending on the order they represent, since higher orders carry fewer energy. An opaque mask, shaded in *grey*, is used to filter the desired first order

## 2.3 Programmable Radon-Wigner Display

In 1994 Wood and Barry proposed to use the RWT instead of the WD to analyze a multicomponent linear FM signal [Woo94]. While the signal components are entangled in the WD representation, they are easily identified in the RWT as local intensity maxima. This idea, originally developed for the analysis of the temporal behaviour of electrical signals, was promptly imported to the analysis of spatial behaviour of optical signals. The first optical RWD [Men96] consisted in two Fresnel zone plates,  $Z_1$  and  $Z_2$ , and a charge-coupled device (CCD) camera separated by a fixed distance  $z$ , see Fig. 2.4a. Each Fresnel zone plate is divided in channels as illustrated in Fig. 2.4b, with each channel implementing a 1D lens of different power.

This RWD is based in the type II Lohmann FRFT optical system, recall Fig. 1.6b. The main difference is that the variable free-space propagation of the FRFT system is replaced in the RWD by an equivalent optical system whose elements do not require to be displaced in order to achieve different FRFT angles. It is easy to demonstrate by ABCD-matrix multiplication that the system formed by three lenses of focal length  $z$ ,  $f$ , and  $z$ , respectively, separated by a distance  $z$  presented in Fig. 2.5 is equivalent to a free-space propagation for distance  $z' = z(2 - \lambda/f)$  [Loh95, Men96]:

$$\begin{aligned}
 & \begin{bmatrix} 1 & 0 \\ -\frac{\lambda}{z} & 1 \end{bmatrix} \begin{bmatrix} 1 & \frac{z}{\lambda} \\ 0 & 1 \end{bmatrix} \begin{bmatrix} 1 & 0 \\ -\frac{\lambda}{f} & 1 \end{bmatrix} \\
 & \times \begin{bmatrix} 1 & \frac{z}{\lambda} \\ 0 & 1 \end{bmatrix} \begin{bmatrix} 1 & 0 \\ -\frac{\lambda}{z} & 1 \end{bmatrix} = - \begin{bmatrix} 1 & \frac{z(2-\frac{\lambda}{f})}{\lambda} \\ 0 & 1 \end{bmatrix}. \quad (2.11)
 \end{aligned}$$

This equivalence allows replacing the variable propagation distance for different FRFT angles into a fixed-distance system with variable focal lenses. Embedding this system into two thin lenses of equal focal length,  $f = f_0 \cot(\gamma/2)$ , and setting  $z' = f_0 \sin \gamma$ , the FRFT of type II for angle  $\gamma$  is obtained. Since we are only interested in the intensity distribution at the output plane of the system, the third lens is not required. Each channel of the RWD performs the FRFT for certain angle using the same approach. If the angles are chosen to cover the range  $[\pi/2, 3\pi/2]$ , the intensity at the output of the optical system corresponds to the full-range RWT of the input signal. Unfortunately, the lenses generated by Fresnel zone plates produce distortions to the incident beam and multiple foci, which reduce the quality of the RWT.

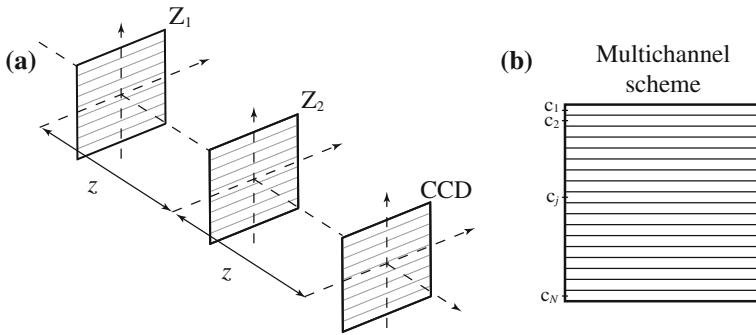


**Fig. 2.4** **a** First optical RWD implementation consisting in two Fresnel zone plates,  $Z_{1,2}$  separated by a fixed distance  $z$ . The beam full-range RWT can be measured at the output plane, which is placed at a distance  $z$  from the second Fresnel zone plate. **b** Detail of the multichannel optical system elements, where  $c_j$  represents the  $j$ th channel

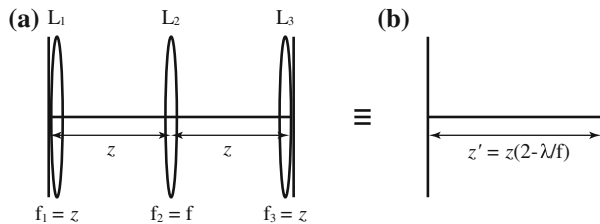


**Fig. 2.5** Equivalent optical systems. **a** Optical system composed by three spherical convergent lenses,  $L_{1,2,3}$ , with focal lengths  $z$ ,  $f$ , and  $z$ , respectively, separated by the same distance  $z$ . **b** Free-space propagation for distance  $z' = z(2 - \lambda/f)$

An alternative RWD avoiding the use of Fresnel zone plates was proposed in [Gra97]. It consists in a cylindrical and a varifocal lens and circumvents the zone plate distortions. The RWTs measured with the system present, however, a significant inconvenience: each WD projection has a different magnification. This means that a pre-process of the RWT to compensate the magnifications is required prior to the WD reconstruction. Moreover, the projections are measured with different resolution by a digital camera, which affects the WD recovery. Another RWD proposal, based on the use of varifocal lenses, prevented the different magnification [Zha98] but required the measurement of the RWT in a curved surface, unsuitable for the use of conventional cameras. Despite the successful analysis performed by these systems, they have not been widely applied.

In order to avoid most of the previous inconveniences, we propose [Cám11a] a RWD without significant projection distortions which provides RWTs with uniform magnification. It is based on the original optical system proposed by Mendlovic et al. [Men96] but with two important differences:

1. SLMs are used to implement the phase masks instead of Fresnel zone plates.
2. Additional cylindrical lenses are included to compensate the beam free-space propagation in the  $y$  direction.

The proposed RWD is versatile because it uses SLMs which can be programmed. This allows, for example, taking multiple RWTs for partial angular range and assemble them into a full angular range RWT with increased number of projections. Moreover, as we will see in Chap. 5, the same configuration of SLMs, without the cylindrical lenses, can be programmed to obtain the WD projections of 2D beams.

An illustration of the proposed system is displayed in Fig. 2.6a. It consists in two SLMs separated a fixed distance  $z$ , and two cylindrical lenses of focal length  $z/4$  with phase modulation in the  $y$  direction also separated a fixed distance  $z$ . The SLMs implement the multichannel phase masks that were originally implemented by Fresnel zone plates in [Men96]. Each channel of the phase mask can be programmed to perform the FRFT operation for an arbitrary angle in the range  $[\pi/2, 3\pi/2]$ . In order to acquire the full-range RWT for  $N$  equidistant angles, the  $j$ th channel of the  $i$ th SLM implements the transmission function  $t_i(x, j)$  given by:

$$t_1(x, j) = \exp[i\Psi_1(\mathbf{r})] = \exp\left[-i\pi \frac{x^2}{\sigma^2} \left(2 - \cot \frac{\gamma_j}{2}\right)\right], \quad (2.12)$$

$$t_2(x, j) = \exp[i\Psi_2(\mathbf{r})] = \exp\left[-i4\pi \frac{x^2}{\sigma^2} (1 - \sin \gamma_{N-j+1})\right], \quad (2.13)$$

where  $j = 1, \dots, N$ ,  $\gamma_j = \pi/2 + (j-1)/N\pi$  is the FRFT angle associated with the  $j$ th channel, and  $\sigma = \sqrt{2\lambda z}$  is the scale parameter of the system. Phase masks corresponding to  $z = 1$  m are displayed in Fig. 2.6b. The initial and final SLM rows are filled with phase masks corresponding to the first and last FRFT angles, respectively, in order to avoid edge effects, see Fig. 2.6b. Consequently, the meaningful area of the intensity distribution at the RWD output plane, which corresponds to the



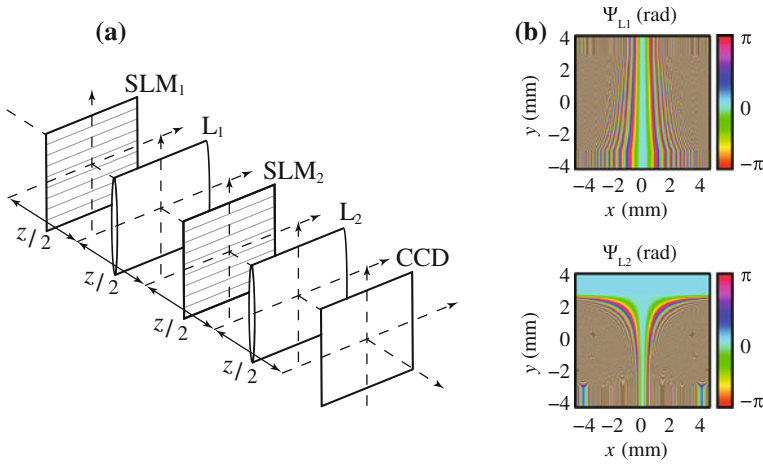


**Fig. 2.6** **a** Implementation of the RWD consisting in two SLMs, SLM<sub>1</sub> and SLM<sub>2</sub>, and two cylindrical lenses, L<sub>1</sub> and L<sub>2</sub>. **b** Phase masks implemented by the SLMs. The FRFT angle changes in the vertical direction

RWT, has to be extracted. While the SLMs perform the FRFT in the  $x$  direction, the cylindrical lenses compensate the beam propagation in the  $y$  direction by imaging the first SLM into the second, and the second into the output plane. Notice since the first cylindrical lens inverts the channel position, the  $j$ th channel of the second SLM implements the angle labelled by  $N - j + 1$  in Eq. (2.13). At the output plane, placed at a distance  $z/2$  from the last cylindrical lens, a CCG camera registers the RWT of the input signal.

The use of SLMs, which compared with Fresnel zone plates or varifocal lenses are more expensive optical elements, is justified by the high versatility of the resulting RWD. In particular, a key advantage of the system is that we can increase the number of WD projections in the RWT by measuring multiple partial angular range RWTs. For example, instead of registering the full-range RWT for  $N$  equidistant angles, it is possible to measure two RWTs of  $N$  equidistant angles covering the ranges  $[\pi/2, \pi)$  and  $[\pi, 3\pi/2)$ , which result in a full-range RWT with  $2N$  projections. As we have seen before, c.f. Fig. 1.9, we will experimentally verify that increasing the number of projections is beneficial for the WD reconstruction. The effects of single-shot, only one RWT measurement, and double-shot, two measurements, are investigated in the experimental results.

Each channel of the RWD expects at its input plane a copy of the 1D signal to be analyzed. These multiple copies can be obtained from a 1D profile of a 2D beam using the setup proposed in [Aga00], which is reproduced in Fig. 2.7. It relays in a slit mask to filter the desired profile and its further expansion using cylindrical lenses. An inconvenience of this system is that the slit diffraction alters the results and drastically reduces the power carried by the signal that has to be processed by the RWD.

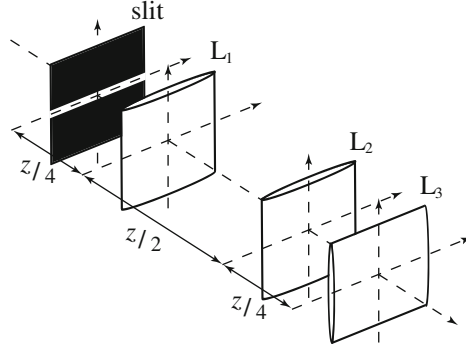


**Fig. 2.7** Optical system proposed in [Aga00] for converting a 1D profile of a 2D beam into the signal expected by the RWD, which is a multiple copy of the profile along the  $y$  direction. It consists in a slit and three cylindrical lenses. The slit is responsible for selecting a profile of the 2D beam. Lenses  $L_1$  and  $L_2$  implement a 4-f telescope for the  $x$  direction. Lens  $L_3$  expands the profile in the  $y$  direction. The cylindrical lenses  $L_1$  and  $L_2$  have the same focal length  $f_1 = f_2 = z/4$  and are separated a distance  $z/4$  and  $3z/4$  from the slit plane. They have the phase modulation axis in the  $x$  direction. The final cylindrical lens,  $L_3$ , with focal length  $f_3 = z$ , is placed at a distance  $z$  from the slit and has the phase modulation axis in the  $y$  direction

## 2.4 Experimental Results

The proposed programmable RWD has been created using two Holoeye LC-R 2500 reflection SLMs with resolution  $1024 \times 768$ , pixel pitch  $19 \mu\text{m}$ , and 8-bit dynamic range; a Ophir-Spiricon SP620U CCG camera of resolution  $1600 \times 1200$ , pixel pitch  $4.4 \mu\text{m}$ , and 12-bit dynamic range; and two cylindrical thin lenses of focal length  $0.25 \text{ m}$ . The collimated beam from a Nd:YAG laser of  $\lambda = 532 \text{ nm}$  illuminates the first SLM. A custom MATLAB package has been developed for the automatized setup manipulation and processing of the acquired data.

In order to test our RWD implementation we experimentally measured the full-range RWT of several 1D test signals: window, windowed chirp, 1D HG beam, and the radial profile of a 2D rotationally invariant beam. The WD of these signals are reconstructed from the full-range RWT for  $\gamma \in [\pi/2, 3\pi/2)$  applying the filtered back-projection algorithm, see Sect. 1.5. For the experimental verification of the proposed scheme we skip the step of 1D signal expansion that, as it has been explained, can be performed using the additional setup displayed in Fig. 2.7. Instead, we generate the input signals in the first SLM of the RWD using a phase-only CGH as explained in Sect. 2.2. Notice that the tasks of lens multiplication and beam generation are performed by implementing a hologram encoding the product of the desired signal,  $f$ , and the RWD phase mask:

$$f_{\text{SLM1}}(x, y) = f(x) t_1(x, j), \quad (2.14)$$

where  $j$  is the channel associated with the value of the vertical coordinate  $y$ .

The first test beam for the experimental demonstration of our RWD is a window signal  $\text{rect}(x/w)$  with  $w = 2.47$  mm, where  $\text{rect}$  is the rectangle function defined by

$$\text{rect}(x) = \begin{cases} 1, & \text{if } |x| < 1, \\ 1/2, & \text{if } |x| = 1, \\ 0, & \text{otherwise.} \end{cases} \quad (2.15)$$

Its full-range RWT is obtained from a single-shot intensity measurement consisting in 293 WD projections for equidistant angles in the interval  $[\pi/2, 3\pi/2]$ . Since the pixel pitch of the SLM is larger than the pixel pitch of the CCG camera, four intensity rows of the acquired RWT correspond to a single channel in the SLM. Therefore, the rows are averaged to obtain the final RWT. To avoid a possible power inequality for different fractional power spectra in the RWT, each WD projection is normalised to unity power. This is justified by the Parseval theorem as introduced in Eq. (1.55). Finally, the acquired data has been processed using the filtered back-projection algorithm yielding the WD of the test beam.

The experimental RWT and WD are compared with the theoretical ones in Fig. 2.8. The good agreement between the theoretically predicted and the experimental results proves the feasibility of the RWD. In particular, several WD fringes are clearly observed above and below the main lobe of the WD. Notice that the method allows reconstructing the negative values of the WD observed as blue colours in Fig. 2.8b which is required for performing a quantitative characterization of the beam. Concretely, the beam MI can be obtained from the WD applying Eq. (1.17).

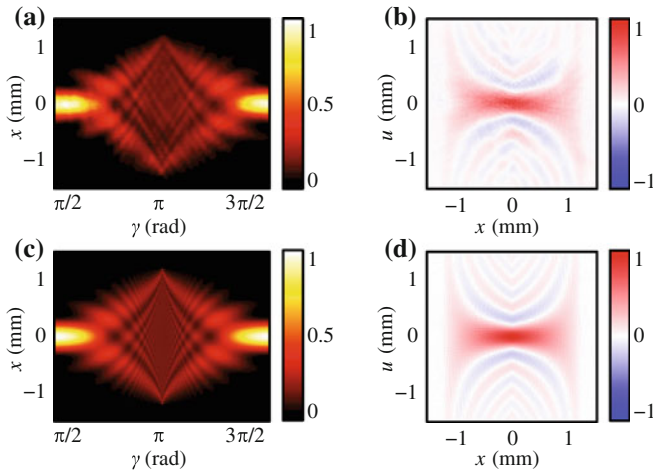


**Fig. 2.8** **a** Experimental single-shot full-range RWT consisting in  $N = 293$  WD projections of a window signal with  $w = 2.47$  mm. **b** Experimental WD reconstructed from the RWT. **c** Simulated RWT consisting in the same projections for the window signal. **d** Simulated WD for the window signal. Notice that both WDs present the negative values characteristic of coherent beams

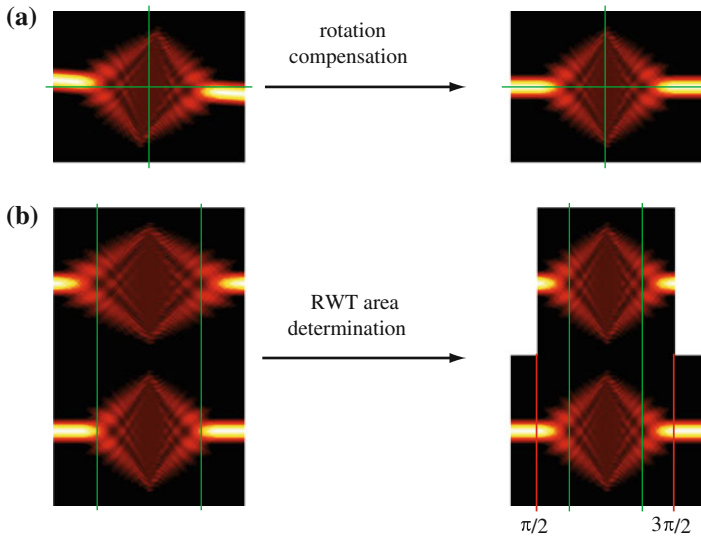


**Fig. 2.9** Illustration of the RWD calibration process. The concrete area of the RWT is obtained comparing the measured RWT with the theoretical expected one. The WD projections associated with the angles  $\pi/2$  and  $3\pi/3$  are determined by resizing the theoretical RWT until some characteristic of both RWTs are aligned. *Green lines* going through the first and last projections of null intensity in their centre are used in this example (Color figure online)

The extraction of the full-range RWT from the measured intensity distribution requires a prior calibration of the RWD. In the case of the window signal it has been performed comparing the theoretically expected RWT with the measured intensity distribution as illustrated in Fig. 2.9. The WD projections associated with the angles  $\pi/2$  and  $3\pi/3$  are determined by resizing the angular axis of the theoretical RWT until some characteristic of both RWTs are aligned. In our case we use as characteristics the first and last projections with zero intensity in their centre, see green lines in Fig. 2.9. This calibration process allows defining the region of interest corresponding to the RWT for other signals. The procedure is also crucial for assembling full-range RWTs in double- or multiple-shot experiments.

In order to explore the benefits associated with the versatility of SLMs, we characterise a more complex beam: a windowed chirp. This signal is described by the complex amplitude  $f(x) = \text{rect}(x/w) \exp[i\pi x^2/(\lambda f_c)]$ . For the experiments we set the window width and the chirp parameter as  $w = 2.47$  mm and  $f_c = 0.93$  m, respectively. In a first experiment we measure a full-range RWT with 293 projections by a single shot, see Fig. 2.10a, from which the WD is reconstructed, see Fig. 2.10b.

In a second experiment we measure a full-range RWT by two shots. This means that from two measurements of the RWT for ranges  $[\pi/2, \pi)$  and  $[\pi, 3\pi/2]$  with 293 WD projections each one, a full-range RWT with 586 WD projections is assembled, see Fig. 2.10c. As in the previous experiment, we reconstruct the WD, which is displayed in Fig. 2.10d. The critical step in the double-shot experiment is the assemblage

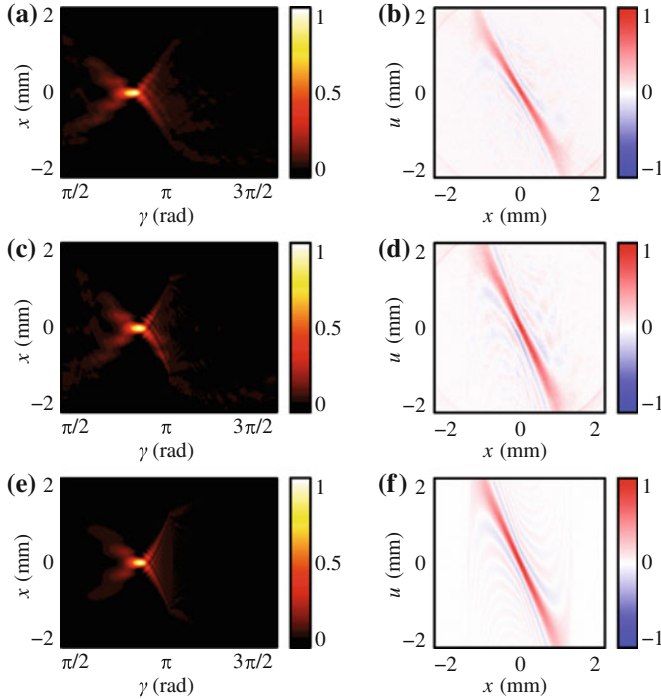


**Fig. 2.10** **a** Experimental single-shot RWT consisting in 293 WD projections in the  $[\pi/2, 3\pi/2]$  range of a windowed chirp signal with  $w = 2.47$  mm and  $f_c = 0.93$  mm. **b** Experimental WD reconstructed from the RWT. **c** Experimental RWT obtained by assembling two single-shot RWTs each consisting in 293 WD projections in the  $[\pi/2, \pi)$  and  $[\pi, 3\pi/2)$  ranges, respectively. **d** Experimental WD reconstructed from the double-shot RWT. **e** Simulated RWT containing the same projections as in the double-shot experiment. **f** Simulated WD for the windowed chirp signal. Notice that, as expected, all the WDs present negative values

of the WD projections obtained in both measurements into the full-range RWT. This is accomplished following the calibration process mentioned above.

In order to better compare the quality of the measured RWTs and reconstructed WDs for single- and double-shot experiments, the theoretically expected RWT and WD are presented in Fig. 2.10e, f, respectively. Since the double-shot RWT contains more information of the beam than the single-shot RWT, its reconstructed WD presents greater fidelity with the theory expectation. This can be appreciated comparing Fig. 2.10b, d, where the fine details around the main lobe are better resolved for the double-shot case. This quality improvement is reflected in a better accuracy of the beam characteristics extracted from the RWT and the WD, as we will see further.

Both the measured RWT and the reconstructed WD contain all the information of the beam spatial structure. Indeed, as it has been mentioned in [Woo94], the chirp parameter is easily obtained from the RWT by finding the FRFT angle associated with the narrower WD projection,  $\gamma_k$ , see Fig. 2.11. The relation between the chirp parameter and  $\gamma_k$  is given by

$$f_c(\gamma_k) = -\frac{\sigma^2}{\lambda} \tan \gamma_k. \quad (2.16)$$

Neglecting all factors contributing to the measurement precision except the finite separation between angles,  $\Delta\gamma_k$ , the chirp parameter precision is calculated as:

$$\Delta f_c(\gamma_k) = \left| \frac{df_c(\gamma_k)}{d\gamma_k} \right| \Delta\gamma_k = \frac{\sigma^2 \Delta\gamma_k}{\lambda \cos^2(\gamma_k)}. \quad (2.17)$$

Notice that when the FRFT angles are equidistant,  $\Delta f_c$  depends indirectly on the total number of projections of the RWT,  $N$ , since  $\Delta\gamma_k = \pi/N$ . Hence, increasing the number of WD projections contained in the RWT, for example performing a double-shot experiment, is a convenient way to make the chirp parameter estimation more precise.

The chirp parameters obtained from the measured RWTs in single- and double-shot experiments are summarized in Table 2.1. Notice that the precision of the double-shot experiment is higher than the precision of the single-shot experiment. In both cases, however, the precision is overestimated since the contributions related to the calibration of the RWT and the errors associated with the chirp generation using a CGH are being ignored. That explains why none of the chirp parameter estimations is compatible with the expected value. Nevertheless, this analysis proves that increasing the number of shots to measure the RWT, and thus effectively increasing the number of WD projections in the RWT, beam characteristics with higher precision can be recovered.

**Fig. 2.11** Illustration of the quantities required to estimate the chirp parameter from the measured RWT. The *green line* is a visual aid to estimate the  $\gamma_k$  angle (Color figure online)

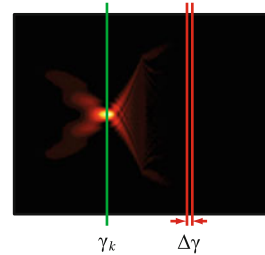


**Table 2.1** Chirp parameter with its associated precision obtained from the single-shot and double-shot experiments and expected by theory

	Chirp parameter	
	$f_c$ (mm)	$\Delta f_c$ (mm)
Single-shot	1.09	0.03
Double-shot	0.905	0.014
Theory	0.93	

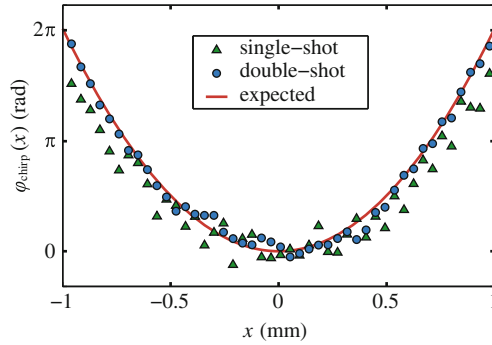


**Fig. 2.12** Phase distributions of the chirp signal relative to the origin point,  $x_0 = 0$ . (Triangle,  $\Delta$ ) Experimental phase distribution for the single-shot RWT consisting in 293 WD projections. (Circle,  $\circ$ ) Experimental phase distribution for the double-shot RWT consisting in 586 WD projections. (Line) Theoretically expected phase distribution

In addition to beam characteristics, like the chirp parameter, local information of the spatial structure of the beam can be extracted from the reconstructed WD. In particular, from the MI obtained by applying Eq. (1.17), the beam phase distribution is directly recovered. The phase distribution relative to the point  $x_0 = 0$ , i.e.  $\arg\Gamma(x, x_0)$ , is compared between the single- and double-shot experiments with theoretical expectation in Fig. 2.12. As opposed to the global information included in the signal parameters, the phase distribution provides local information, which is important for numerous applications for example in microscopy.

The proposed method and system is not only working in simple signals like the window and windowed chirp examples. The same procedure can be applied to obtain the WD of other signals. For instance, in Figs. 2.13 and 2.14 there are displayed, respectively, the theoretical and experimental WDs of:

- the 1D HG mode  $\mathcal{H}_4(x)$  for  $w = \sigma = 0.72$  mm, and
- the radial profile ( $y = 0$ ) of the combination of LG modes  $f_{\text{LG}}(\mathbf{r}) = \mathcal{L}_0^0(\mathbf{r}) + 2\mathcal{L}_2^0(\mathbf{r})$  with  $w = \sigma = 0.72$  mm.

It is evident, when analyzing its RWT, that the HG beam is an eigenfunction of the FRFT operator since all its WD projections present the same form. This is reflected in the WD by its rotationally invariant structure. It also means that the beam preserves its shape during free-space propagation. This is not the case for the radial profile of the  $f_{\text{LG}}$  beam because its projections are not identical. Notice that since  $f_{\text{LG}}$  is rotationally invariant we can obtain its 4D WD from the WD of its radial projection following the procedure proposed in [Aga00].

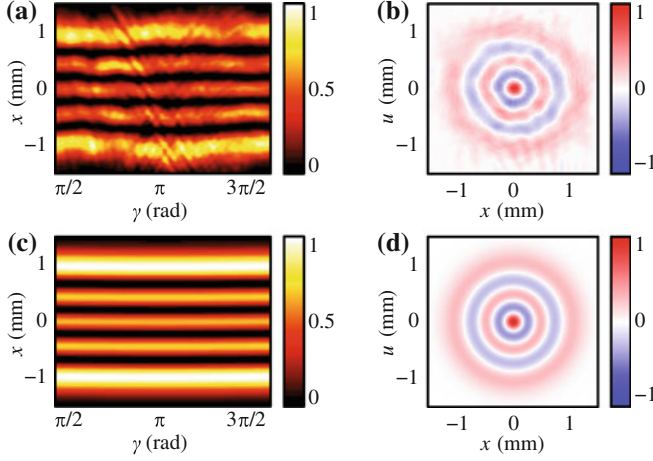


**Fig. 2.13** Analysis of the  $\mathcal{H}_4(x)$  beam with  $w = 0.72$  mm. **a** Experimental single-shot full-range RWT consisting in 293 WD projections. **b** Experimental WD reconstructed from the RWT. **c** Simulated RWT. **d** Simulated WD

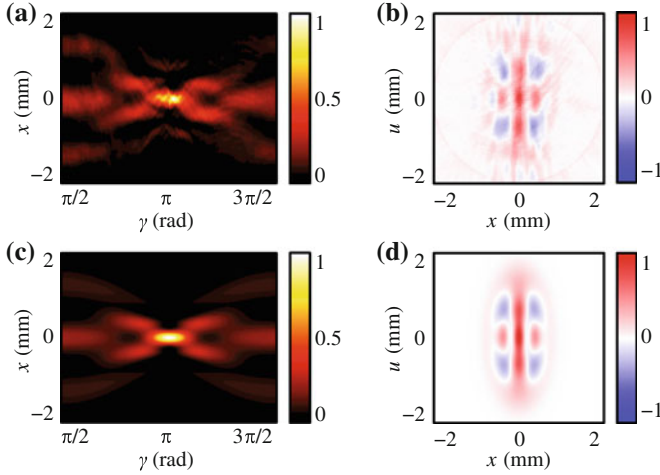


**Fig. 2.14** Analysis of the radial profile of the combination  $\mathcal{L}_{0,0} + 2\mathcal{L}_{2,2}$  with  $w = 0.72$  mm. **a** Experimental double-shot full-range RWT consisting in 586 WD projections. **b** Experimental WD reconstructed from the RWT. **c** Simulated RWT. **d** Simulated WD

## 2.5 Conclusions

The good agreement between the experimental results and the theoretical expectations allows concluding that the proposed RWD is feasible for the analysis of 1D signals. In particular, this includes the characterization of pure 1D signals and 1D profiles of 2D beams. Furthermore, the WD of 2D rotationally invariant beams can



be recovered from the WD of its radial profile via [Aga00]. Although the experimental results were obtained for completely coherent beams, the method is coherence agnostic and should be equally feasible for partially coherent beams.

The exploration of double-shot experiments to determine the beam RWT has lead us to important results. Indeed, performing multiple shots assembled into the full-range RWT increases the number of its WD projections, which in turn improves the quality of the WD reconstruction and precision of the quantitative beam characterization. The single- and double-shot experiments have been studied for the case of a windowed chirp signal. Although it is reasonable to think that the WD quality will improve for more than two shots, this improvement is limited by the errors introduced in the calibration process. Moreover, since the information is not obtained from a single measurement, it cannot be used for processes that rapidly change in time.

Another advantage of using the suggested RWD is its ability to centre the beam analysis in certain RWT region of interest. For example, consider that we already knew that the chirp parameter of an unknown signal is around certain FRFT angle,  $\gamma$ . Then, instead of measuring a single-shot full-range RWT, we could measure the single-shot RWT for range  $[\gamma - \epsilon, \gamma + \epsilon)$  where  $\epsilon$  defines the region of interest. This procedure is trivial to perform using the proposed RWD and leads to more precise beam characterization.

Unfortunately, these advantages are only pertinent to the characterization of 1D beams. For the more general case of 2D signals, different simplified methods are proposed. For instance, in the following chapters, the method for the analysis of 2D signals that are separable in Cartesian coordinates is explored. As we will demonstrate, in a certain way 2D separable beams are similar to 1D beams.

Most of the results of this chapter are published in [Cám11b] and were presented at the congresses [Cám11a, Cám11c].

## References

- [Aga00] G.S. Agarwal, R. Simon, Reconstruction of the Wigner transform of a rotationally symmetric two-dimensional beam from the Wigner transform of the beam's one-dimensional sample. *Opt. Lett.* **25**(18), 1379–1381 (2000)
- [Arr07] V. Arrizón, U. Ruiz, R. Carrada, L.A. González, Pixelated phase computer holograms for the accurate encoding of scalar complex fields. *J. Opt. Soc. Am. A* **24**(11), 3500–3507 (2007)
- [Bon90] D. Bonaccini, G. Brusa-Zappellini, S. Esposito, P. Salinari, P. Stefanini, Adaptive optics wavefront corrector using addressable liquid crystal retarders. *SPIE Proc.* **1543**, 89–97 (1990)
- [Cám11a] A. Cámara, T. Alieva, J.A. Rodrigo, M.L. Calvo, Optical systems and algorithms for phase-space tomography of one- and two-dimensional beams. in *22nd Congress of the ICO* (2011)
- [Cám11b] A. Cámara, T. Alieva, J.A. Rodrigo, M.L. Calvo, Phasespace tomography with a programmable Radon-Wigner display. *Opt. Lett.* **36**(13), 2441–2443 (2011)
- [Cám11c] A. Cámara, T. Alieva, J.A. Rodrigo, M.L. Calvo, Radon-Wigner display implemented by spatial light modulators. in *PIERS Proceedings* (2011)

- [Dit96] T. Ditmire, E.T. Gumbrell, R.A. Smith, J.W.G. Tisch, D.D. Meyerhofer, M.H.R. Hutchinson, Spatial coherence measurement of soft X-ray radiation produced by high order harmonic generation. *Phys. Rev. Lett.* **77**, 4756–4759 (1996)
- [Goo05] J.W. Goodman, *Introduction to Fourier Optics* (Roberts & Company, Colorado, 2005)
- [Gra97] S. Granieri, W.D. Furlan, G. Saavedra, P. Andres, Radon-Wigner display: a compact optical implementation with a single varifocal lens. *Appl. Opt.* **36**(32), 8363–8369 (1997)
- [Loh95] A.W. Lohmann, A fake zoom lens for fractional Fourier experiments. *Opt. Commun.* **115**(5–6), 437–443 (1995)
- [Men96] D. Mendlovic, R.G. Dorsch, A.W. Lohmann, Z. Zalevsky, C. Ferreira, Optical illustration of a varied fractional Fourier-transform order and the Radon-Wigner display. *Appl. Opt.* **35**(20), 3925–3929 (1996)
- [Nei00] M.A.A. Neil, R. Juškaitis, M.J. Booth, T. Wilson, T. Tanaka, S. Kawata, Adaptive aberration correction in a two-photon microscope. *J. Microsc.* **200**(2), 105–108 (2000)
- [Oht99] S. Ohtaki, N. Murao, M. Ogasawara, M. Iwasaki, The applications of a liquid crystal panel for the 15 Gbyte optical disk systems. *Jpn. J. Appl. Phys.* **38**(Part 1, No. 3B), 1744–1749 (1999)
- [She91] M.H. Sher, S.J. Benerofe, J.F. Young, S.E. Harris, 2-Hz 109-nm mirrorless laser. *J. Opt. Soc. Am. B* **8**(1), 114–116 (1991)
- [Woo94] J.C. Wood, D.T. Barry, Linear signal synthesis using the Radon-Wigner transform. *IEEE Trans. Signal Process.* **42**(8), 2105–2111 (1994)
- [Wul06] K.D. Wulff, D.G. Cole, R.L. Clark, R. DiLeonardo, J. Leach, J. Cooper, G. Gibson, M.J. Padgett, Aberration correction in holographic optical tweezers. *Opt. Express* **14**(9), 4169–4174 (2006)
- [Zha98] G. Yan Zhang, B.-Z.D. Ben-Yuan, G.-Z. Yang, Optical implementations of the Radon-Wigner display for one-dimensional signals. *Opt. Lett.* **23**(14), 1126–1128 (1998)

Optical Beam Characterization via Phase-Space  
Tomography

Cámara, A.

2015, XIV, 114 p. 58 illus., 27 illus. in color., Hardcover

ISBN: 978-3-319-19979-5